HHS Public Access

Author manuscript

Magn Reson Med. Author manuscript; available in PMC 2021 July 01.

Published in final edited form as:

Magn Reson Med. 2020 July ; 84(1): 289–303. doi:10.1002/mrm.28131.

First In-Vivo Human Imaging at 10.5T: Imaging the Body at 447 MHz

Xiaoxuan He[1], **Arcan Ertürk**[1], **Andrea Grant**[1], **Xiaoping Wu**[1], **Russell L. Lagore**[1], **Lance DelaBarre**[1], **Yiğitcan Eryaman**[1], **Gregor Adriany**[1], **Eddie Auerbach**[1], **Pierre-François van de Moortele**[1], **Kâmil Uğurbil**[1], **Gregory J. Metzger**[1,*]

[1]Center for Magnetic Resonance Research, University of Minnesota, Minneapolis, Minnesota, United States

Abstract

Purpose—To investigate the feasibility of imaging the human torso and to evaluate the performance of several RF management strategies at 10.5T.

Methods—Healthy volunteers were imaged on a 10.5T whole-body scanner in multiple target anatomies, including the prostate, hip, kidney, liver, and heart. Phase-only shimming and spoke pulses were used to demonstrate their performance in managing the B_1^+ inhomogeneity present at 447 MHz. The imaging protocols included both qualitative and quantitative acquisitions to show the feasibility of imaging with different contrasts.

Results—High-quality images were acquired and demonstrated excellent overall contrast and SNR. The experimental results matched well with predictions and suggested good translational capabilities of the RF management strategies previously developed at 7T. Phase-only shimming provided increased efficiency but showed pronounced limitations in homogeneity demonstrating the need for the increased degrees of freedom made possible through single-spoke and multi-spoke RF pulse design.

Conclusion—The first in-vivo human imaging was successfully performed at 10.5T using previously developed RF management strategies. Further improvement in the RF coils, transmit chain, and full integration of parallel transmit functionality are needed to fully realize the benefits of 10.5T.

Keywords

10.5T; Body Imaging; Parallel Transmit; Ultra-High Field Imaging; Magnetic Resonance Imaging

INTRODUCTION

Since the introduction of the first 7T whole-body human MRI (1)(2), the last two decades have seen a significant increase in utilization of ultra-high field (UHF) scanners in human research, eventually paving the way to the recent approval of 7T for clinical use. However,

[*]**Corresponding Author:** Gregory J. Metzger, Ph.D. (gmetzger@umn.edu), Center for Magnetic Resonance Research, University of Minnesota, 2021 6th Street SE, Minneapolis, MN 55455, United States.

the enthusiasm for increasing field strengths continues beyond 7T. Before the arrival of the 10.5T whole-body scanner at the University of Minnesota, several systems greater than 7T have effectively demonstrated improved human imaging and spectroscopy (2–6). While the majority of 7T work has focused on applications in the head, the feasibility and advantages of musculoskeletal and torso imaging at UHF have also been demonstrated (7,8). Although UHF imaging is generally challenging, the motivation is driven primarily by the observation that the sensitivity of MRI increases with field strength (1,9). Sensitivity gains can potentially contribute to higher spatial resolution providing richer anatomical and functional detail or contribute to improved acquisition efficiency in cases where signal averaging is required, especially with the low sensitivity of non-proton nuclei. Additional and significant advantages of UHF also include increased parallel imaging performance (10,11), spectral dispersion (12) and quantification (13), and greatly improved contrast to noise ratios in susceptibility weighted anatomical imaging (13–16) and in functional mapping of the brain (17). Many of these advantages promise to provide new insights into biological structure and function as well as to increase the sensitivity and resolution of biomarkers for accessing metabolic information in the brain and body.

Harnessing the power of UHF, however, has not been straightforward, involving a combination of RF hardware, RF management, and methodological developments. Since its introduction, a major challenge of UHF imaging is the transmit B1 (B_1^+) inhomogeneities observed as signal non-uniformities due to the shorter RF wavelengths in tissues resulting in destructive interference patterns(1,18–20). This problem can be ameliorated or corrected using parallel transmit instrumentation (18,21) together with various strategies such as B_1^+ phase and/or amplitude shimming (18,22–24), transmit SENSE (e.g., (25–28)), spoke pulses (e.g., (24,29–32)), k-T pulses (33), etc., to generate uniform flip angles over a targeted region.

The aforementioned concepts for dealing with B_1^+ inhomogeneities are widely adopted in both brain and body imaging at 7T. However, with an even shorter within-tissue wavelength of approximately 7cm at 10.5T, it was unclear how well the RF management methods previously developed at 7T would mitigate the field strength-dependent challenges at 10.5T, especially in the human torso.

Another critical concern at UHF is local RF heating as a result of higher peak local specific absorption rates (SAR) and reduced SAR efficiency, $B_1^+/(SAR)^{0.5}$. To safely manage the power delivered to the body, power limits derived from electromagnetic simulations validated by experimental studies are required (34). In combination, the tradeoff between the maximum achievable B_1^+, transmit homogeneity, and local SAR needs to be carefully considered as all three can compromise final image SNR and contrast. The sweet spot where a reasonable solution can be found for all three narrows with increasing field where optimizing for one characteristic can compromise the others.

Local transmitters close to the surface of the body have been the preferred approach for UHF imaging in the human torso. While in some recent cases these local transmit arrays have been paired with separate receive-only elements (35–38), many often still operate solely as transceiver arrays (39–42). In our previous work, we developed a 10-channel transceiver

dipole array (43) for 10.5T body imaging and reported simulation results and experimental data obtained with a human-torso sized phantom. This relatively simple RF torso array, where each element is heavily loaded by the body and far from its neighbors, was straightforward to validate and thus was approved for human imaging by the FDA prior to any RF coil designed for the head. Using this array, human imaging was possible as an additional component to an ongoing 10.5T safety study, allowing us to explore the feasibility and challenges of imaging the human torso at 447MHz. Therefore, although imaging human brain function and anatomy remains the primary motivation for the development of the 10.5T system, the body images shown in this work were from the first human studies performed at this field strength, with the very first acquisition targeting the prostate (Supporting Information Figure S1 *available online*).

In this preliminary investigation, we acquired data in five anatomies, including the prostate, hip, kidney, liver, and heart, to explore the target and field dependent characteristics of RF management strategies, the ability to implement standard target specific acquisitions, and to determine the extent to which expected contrasts could be obtained. With this work, we demonstrate the potential of 10.5T as a cutting edge, whole-body imaging system using current parallel transmit RF management methods with the overall goal of exploiting such extremely high field strengths to enhance biomedical research and discovery.

METHODS

MRI Scanner

MRI experiments were conducted on a whole-body 10.5T magnet (Agilent Technologies, Oxford, UK) and associated imaging system (Siemens Healthineers, Erlangen, Germany) following an IRB approved protocol with an FDA Investigational Device Exemption (IDE). This passively shielded magnet has a clear bore diameter of 88 cm, is 4.40 m in length and weighs 110 tons. The 4700 L of liquid helium is cooled to 2.3 K to maintain the superconductivity of the magnet conductor which is required to be < 3 K based on the manufacturer's specifications. The field homogeneity of the magnet is <0.07 ppm / 25 cm and can be adjusted by second and third order room temperature shims driven by 20 A amplifiers. The scanner is equipped with 32 receivers, a 16-channel "Step 2" parallel transmit (pTx) system with each channel driven by a 2 kW power amplifier (Stolberg HF-Technik AG, Stolberg, Germany), and a whole-body SC 72 gradient system (Siemens Healthineers, Erlangen, Germany) which can achieve a maximum amplitude of 70 mT/m and slew rate of 200 T/m/s. The patient accessible bore size with the covers in place is 60 cm in diameter.

The dipole array used in this study was interfaced to the scanner by means of a 16-channel interface box which facilitates transmit-receive switching and signal preamplification. To minimize vestibular effects when moving through the static magnetic field (44–47), the speed of the table was limited to 19 mm/s as compared to 38 mm/s typically used at 7T. After RF and B_0 calibration scans, eye tracking and cognitive tests were performed while RF shims and/or pTx pulses were calculated to make full use of the limited amount of time subjects spent at isocenter.

Subject Recruitment

All volunteers who participated in this study provided written informed consent to participate in the FDA and IRB approved safety study. The primary objective of the study was to assess the effects of field exposure on vestibular, cognitive, and physiologic function. The safety data collected during the protocol will be reported separately. In vivo imaging was a secondary objective of the study and was not performed until the subject's second time in the scanner. On the day imaging was to be performed, subjects were in the scanner for 90 min of which approximately 60 min were used for imaging and the rest for safety specific measurements.

Exclusion criteria to 10.5T exposure and imaging were strictly enforced. Subjects were required to have no history of embedded metal, either through surgery or accidentally, while also being free from symptoms or specific diagnosis of vestibular or cognitive impairment. Experience as a subject in a 7T scan was also a requirement for participation in the 10.5T studies. For those subjects who had not previously experienced imaging at 7T, a 7T pre-scan was first conducted to acclimate individuals to scanner procedures and being in a research environment. For body (i.e. torso) imaging, a total of 20 subjects (14/6 males/females) were imaged, ranging in age from 21Y to 65Y (36.95 ± 13.87), in weight from 56.7 kg to 102.06 kg (75.11 ± 13.37) and in BMI from 19.53 kg/m^2 to 33.47 kg/m^2 (25.33 ± 3.53). The permitted size of subjects allowed in the 10.5T was restricted to the weights of the virtual human models employed for electromagnetic calculations of the RF coil with margins of ±25%. This resulted in a continuous range of allowable weights from 43 to 120 kg.

RF Field Management

Static Phase-only RF Shimming (Phase Shimming)—RF shimming with various cost functions was used to manage the tradeoff between efficiency and homogeneity in the imaged target anatomies. The calibration methods needed for static RF shimming included tools to measure the relative complex B_1^+ from each transmit element of the transceiver array (19,48). This method uses a low flip angle approximation to allow the robust estimation of each transmit channel's spatially varying relative magnitude and phase (49,50). Using these calibration data, phase-only (50) as well as phase and magnitude (phase-magnitude) RF shimming (51) are possible. In the context of this study "phase shimming" will refer only to the phase-only optimization of RF while the phase-magnitude approaches will be addressed through the use of spoke pulses detailed below.

In all cases, phase shimming was performed within a region of interest (ROI) defined on anatomic images by the operator. Depending on the subject and anatomy of interest, optimal channel-dependent properties were determined using a cost function that maximized efficiency, maximized homogeneity, or optimized for a trade-off between the two. For the prostate, phase shimming performance was characterized by the B_1^+ transmit efficiency defined as the ratio of the magnitude of the sum (MOS) to the sum of the magnitude (SOM) of the channel-dependent complex B_1^+ fields acquired from the low flip angle calibration data. Inhomogeneity was measured by the coefficient of variation (CV) of the MOS of B_1^+ within the ROI. All calculations were performed in MATLAB (The MathWorks, Inc.,

Natick, MA) using custom software. Calculated shims were written to a file and read into the transmit array interface on the scanner's host computer.

Spoke Pulses—As an alternative approach to phase shimming, spoke pulses were implemented in which both phases and magnitudes for each channel were designed to minimize transmit field inhomogeneity. While a single spoke pulse is essentially equivalent to a static phase and magnitude shim, the design process and implementation followed the same path as for multi-spoke pulses. Spoke pulses were designed to address field inhomogeneities in larger targets including the kidneys, heart, and liver. As previously described, magnitude least squares optimization (52) with Tikhonov regularization was used to balance between RF power and excitation fidelity. The regularization parameter was automatically determined based on the L-curve criterion using the l_curve() function from the MATLAB regtools package (53). Similar to previous predictions and experimental results at 7T, it was expected that pulses with higher numbers of spokes would provide increased degrees of freedom to better mitigate B_1^+ inhomogeneity at 10.5T (54). The pulse design made use of the same rapidly acquired channel-wise complex B_1^+ map estimates used for phase shimming along with B_0 maps acquired with a standard multi-echo gradient echo acquisition (Supporting Information Tables S1 and S2 *available online*).

Peak Achievable B1+ in the Prostate—The actual flip angle imaging method (AFI) (55) was used to measure B_1^+ in the prostate and for estimating peak achievable B_1^+ given the complete transmit chain. The maximum achievable B_1^+ was calculated by rescaling the measured B_1^+ by the maximum transmitter voltage available on the scanner. A linear regression was conducted to characterize the peak B_1^+ empirically in the anterior-posterior dimension of the subjects. Direct measurements of B_1^+ and estimates of peak achievable B_1^+ were performed in the prostate due to the limited motion present in this anatomical target.

Coil Validation & Establishing Safe Operating Limits

The RF transmit array (coil) used in this study consisted of a previously detailed 10-channel dipole antenna array (43). Prior to in vivo imaging, the coil went through a validation procedure similar to previously published strategies (34). First, electromagnetic (EM) simulations and experimental studies in phantoms were used to demonstrate consistency between the two with respect to magnetic and electric fields. Briefly, for comparison with simulation, experimental B_1^+ maps were acquired with AFI and local SAR values were calculated from fiber optic probe measurements during separate heating studies. Second, to determine safe operating power limits, electromagnetic simulations were performed in the Ella, Duke, and Fats29 virtual family human body models (Sim4Life, Zurich Medtech, Zurich, Switzerland) with the coil appropriately positioned to separately target the heart, mid-torso (kidney and liver), and pelvis (hips, prostate, or uterus) of each model. Using the channel-wise EM-field simulations, phase shimming solutions were determined in each target anatomy across all human body models. For each model and target location, local SAR values averaged over 10 g of tissue (SAR_{10g}) were determined for the static phase-only shim solutions from efficiency to homogeneity. The peak SAR_{10g} value from all models and targets was 0.59 W/kg arising from a total input power of 1 Watt, resulting in a global phase shimming limit of 34 W total power (i.e. 3.4 W per channel) based on the IEC guidelines for

peak local SAR in the torso (i.e. 20 W/kg) (56). In practice, an effective total power limit of 17 W (i.e. 1.7 W per channel) was used, providing a safety factor of 2. This value was deemed to be conservative for initial in vivo studies at 10.5T realizing that the human body model sizes and shapes (57) as well as target size and location (58) impact local SAR estimates.

For spoke-pulses, both single- and two-spoke solutions were determined in each target anatomy across all human body models using the methods detailed above. For the single- and two-spoke solutions, the peak local SAR_{10g} values for a total input power of 1 Watt across all models and targets were 0.90 W/kg and 1.1 W/kg, respectively. Using the same total power limit of 17 W, spoke excitation was performed with a safety factor >2 for the kidney and >10 for the heart and liver due to the acquisition methods and parameters used for imaging (Supporting Information Table S2). In the kidney, >98% of the power deposition was the result of a fat suppression pre-pulse using a default phase shim solution. The spoke pulses delivered <2% of the total power in these acquisitions.

Imaging Protocols

Due to different geometries and motion sensitivities, the resultant protocols for the imaged anatomies differed in terms of slice planning, matrix size and/or triggering strategy (acoustic for heart, respiratory for kidney) as detailed below.

Prostate Imaging—Prostate imaging was performed to investigate the performance of phase shimming at 10.5T. Due to its small size, central location in pelvis, and limited motion, high transmit efficiency and acceptable homogeneity were expected with this RF management approach. The prostate also allowed exploration of multiparametric and quantitative imaging including the acquisition of T_2-weighted and diffusion contrasts typical of standard diagnostic protocols. A multi-slice static phase shimming was performed to optimize B_1^+ efficiency, followed by a combination of the following acquisitions in each subject: AFI B_1^+ mapping, T_2W TSE for anatomy, T_1 mapping using an adiabatic inversion prepared single-shot Turbo-FLASH, T_2 mapping using a CPMG multi-echo spin-echo sequence, and diffusion weighted imaging. Detailed protocol parameters are provided in Supporting Information Table S1. Parametric maps for T_1, T_2, and ADC were calculated by using standard non-linear least squares fitting functions in MATLAB.

Hip Imaging—Hip imaging was performed with larger fields of view than the prostate with phase shimming focused on the cartilage and other soft tissue structures around the femoral head. Initial fat suppressed GRE images allowed the overall image uniformity and fat suppression across the pelvis to be assessed, while typical anatomy-specific acquisitions, including a merged multi-echo gradient echo (MEDIC) (59) and proton density weighted TSE (PD-TSE) acquisition, were performed to assess the ability to obtain clinically relevant contrasts. For phase shimming, bilateral hip imaging is more challenging than the prostate because the ROIs needed for optimization are larger and spatially separated. The acquisition details for the hip studies are included in Supporting Information Table S1.

Kidney Imaging—Kidney imaging included breath-hold, fat-suppressed sequences to visualize anatomy, as well as non-contrast inflow enhanced acquisitions to delineate vessels. Phase shimming in the kidneys is more challenging than in the hips. Despite the fact that both are bilateral structures, the kidneys are larger and more posteriorly positioned in the torso and experience respiratory related motion requiring a breath-hold calibration scan. When visualizing the renal arteries as well as the renal parenchyma, the RF optimization becomes even more complex as the region between the kidneys and the descending aorta also needs to be included (51). Phase shimming was performed on two different ROIs; one ROI including the renal arteries and one excluding the renal arteries. To address the posterior position of the kidneys, the use of single-spoke RF pulses was explored to improve transmit homogeneity and contrast uniformity in the kidneys and renal arteries. Acquisition methods used for this anatomy are provided in Supporting Information Table S2.

Liver Imaging—Liver imaging was performed to explore the limits of transmit homogeneity as it is the largest internal organ in the human body, excluding the interstitium. Phase shimming was compared against single- and two-spoke pulses with respect to B_1^+ uniformity across the liver. This comparison was accomplished by applying the RF management strategies to low flip angle GRE acquisitions and comparing the images with corresponding predicted B_1^+ profiles. Breath-holding was used to reduce respiratory motion artifacts in both the calibration and anatomic imaging experiments. Acquisition parameters are provided in Supporting Information Table S2.

Cardiac Imaging—Cardiac imaging included RF shimming and retrospectively gated GRE CINE imaging of four chamber and short axis views. Cardiac gating was made possible by a previously reported acoustic cardiac trigger (60). Calibration scans were acquired as a single cardiac phase during diastole within a single breath-hold. Phase shimming was compared against single-spoke pulses in a four-chamber CINE acquisition. Detailed acquisition parameters are provided in Supporting Information Table S2.

RESULTS

Prostate Imaging

The local phase shimming ROI was placed around the prostate on three axial slices that were evenly spaced covering the majority of the gland. The estimated B_1^+ profile and efficiency maps before and after shimming along with the acquired low-flip angle GRE images are shown in Figure 1. By using efficiency or tradeoff shimming solutions, the average B_1^+ efficiency increased from 36.0 ± 5.2% prior to shimming to 79.7 ± 4.5% in the 9 prostate subjects, while inhomogeneity decreased from an initial value of 0.486 ± 0.063 to 0.211 ± 0.068, suggesting the effectiveness of using phase shimming to mitigate B_1^+ inhomogeneity for this target. Both axial and coronal T_2W TSE images are shown in Figure 2 to demonstrate the image quality of clinically relevant acquisitions at 10.5T. As an example, a complete set of axial and coronal T_2W TSE images is shown in Supporting Information Figure S2. As part of a multi-parametric study, data were acquired in a subset of participants allowing for calculation of quantitative maps including T_1, T_2, ADC, and high b-value DWI images (Figure 3). The mean T_1 from 3 subjects was 2603 ± 189 ms and the mean T_2 and

ADC from the peripheral zone of 2 subjects were 83.5 ± 2.1ms and 1792 ± 105 (10^{-6} mm^2/s), respectively. The average B_1^+ in the prostate across all subjects was 10.2 ± 1.9 μT, and the average CV was 13.0 ± 2.4%. A linear regression analysis suggested that B_1^+ decreases at a rate of approximately 0.82 μT per cm in anterior-posterior (AP) distance across the pelvis with a maximum B_1^+ of 13.0 μT at an AP dimension of 16.5 cm.

Hip Imaging

Unilateral and bilateral hip imaging were performed in one and two subjects, respectively. The local phase shimming ROIs were drawn by outlining the femoral head and associated cartilage in the coronal and axial planes with a negative ROI removing the bone thus leaving the signal from a thin rim of soft tissue for optimization (61). After phase shimming, the average B_1^+ efficiency increased from 47.8 ± 5.8% to 66.1 ± 7.2% and the average B_1^+ inhomogeneity decreased from 0.697 ± 0.130 to 0.503 ± 0.162. The acquired images are shown in Figure 4 and demonstrate excellent lipid suppression throughout the pelvis, effective mitigation of B_1^+ inhomogeneity in the ROIs, and the ability to visualize fine structures on the 0.7mm isotropic MEDIC images. Important tissue contrast was obtained on the PD weighted images allowing visualization of the labrum.

Renal Imaging

Renal imaging studies were performed in 4 subjects. Shimming ROIs circumscribed each kidney on a set of three axial calibration slices acquired in a single breath hold. The shimming solution was calculated using an efficiency cost function. The average B_1^+ efficiency increased from 46.1 ± 6.8% to 67.9 ± 3.8%, and the average B_1^+ inhomogeneity decreased from 0.494 ± 0.008 to 0.360 ± 0.011. For the vessel imaging acquisitions (4 cases), the ROIs for shimming covered the kidneys and the renal arteries, including the descending aorta (51). In total, the average B_1^+ efficiency increased from 45.4 ± 5.8% to 61.5 ± 3.1%, and the average B_1^+ inhomogeneity decreased from 0.456 ± 0.101 to 0.299 ± 0.047. Inflow-enhanced GRE images were acquired and processed providing maximum intensity projection (MIP) images that demonstrated high inflow contrast and clear visualization of both the proximal and distal renal arteries (Figure 5). Single-spoke RF pulses were compared against the performance of phase shimming at mitigating B_1^+ inhomogeneity. The single-spoke pulse optimized on the larger ROI provided the best depiction of the left and right renal arteries (Figure 6).

Liver Imaging

Due to the limitation of coil positioning, only one subject was included in the liver study. The shimming ROIs were drawn on three evenly spaced axial slices acquired through the liver. Static phase-only shimming optimized for homogeneity resulted in increased B_1^+ efficiency from 0.428 to 0.505 and decreased inhomogeneity from 0.436 to 0.287. Single-spoke and two-spoke pTx pulses were also designed using the same ROIs, and images were obtained to compare against those acquired with the phase shim solution. Simulated and experimental results demonstrated high concordance with greatly improved B_1^+ homogeneity and contrast uniformity over the liver when taking advantage of the increased degrees of freedom afforded by the two-spoke pulse (Figure 7).

Cardiac Imaging

Cardiac imaging was performed in one subject. Phase shimming was performed for short-axis and four-chamber views, yielding an average increase in B_1^+ efficiency from 0.383 ± 0.019 to 0.712 ± 0.063, while keeping almost the same level of inhomogeneity (before: 0.376 ± 0.047 versus after: 0.380 ± 0.059). The CINE images before and after phase shimming showed improved RF efficiency and a shift of the dark RF band to outside of the heart (Figure 8b). Compared with phase shimming, the single-spoke solution mitigated B_1^+ inhomogeneity especially at the atrium and base of ventricle of the heart, as depicted in Figure 8e. The Bloch simulation also showed that the single-spoke solution reduced the inhomogeneity from 0.42 to 0.21 and increased the average flip angle by 27% for the same RF power, all suggesting the importance of incorporating pTx into field and power management.

DISCUSSION

In this study, we performed the first in vivo human imaging at 10.5T (447MHz) with the goal of exploring the feasibility of obtaining images of multiple anatomical targets in the torso at this high magnetic field using the RF management strategies developed for 7 Tesla. The well-known difficulties arising from B_1^+ inhomogeneities associated with decreasing RF wavelengths (19) make torso imaging at 10.5T particularly challenging. While previous simulations had indicated such imaging would be feasible in the human torso at 10.5T (43), there had not been an experimental confirmation to date. In addition, the simulations did not provide insights as to the obtainable image quality or tissue contrasts that could be expected at this extremely high field strength.

In these initial studies with the current RF coil and transmit chain configuration, phase shimming provided sufficient B_1^+ peak performance and homogeneity to perform anatomic and quantitative imaging in the prostate. The small volume and the central position of the prostate in the pelvis enabled this relatively simple strategy, optimized primarily for transmit efficiency, to be successful in most cases. As the anatomical targets in the body increased in size and asymmetry, however, additional degrees of freedom were required, either through single-spoke or multi-spoke RF pulses, to obtain the desired homogeneity in signal and contrast. With increasing constraints on B_1^+ homogeneity, transmit efficiency dropped to a point where it was difficult to obtain some desired contrasts due to the limited peak B_1^+ or SAR efficiency. This fact highlights the need for improved RF coil and transmit chain efficiency as well as further integration of more SAR efficient pTx pulses into standard acquisition strategies.

Despite the limitations with the current coil and phase shimming, quantitative imaging was successfully performed in the prostate. While the T_2 values appear to be in a reasonable range for 10.5T, the reported T_1 values appear longer than expected compared with the limited studies done at 7T (62). ADC values, which should be independent of field strength, also appear to be larger than expected compared to quantitative studies reported at 3T (63). However, for all parameters, the acquisition, subject, and field dependent variability cannot be adequately assessed until more extensive targeted evaluations are performed.

In almost all the studies, RF optimization was conducted immediately following scout acquisitions, serving as an initial B_1^+ field calibration and reference before proceeding with additional acquisitions or the use of different RF management strategies. While phase shimming has limited degrees of freedom compared to other approaches, it remained a fast and effective solution for small ROIs such as the prostate and hips while generally proving capable for both qualitative and, in the prostate, quantitative imaging. Previously, we were able to obtain reasonable results for bilateral hip imaging at 7T (61) using phase shimming. The same approach also provided reasonable bilateral hip images at 10.5T; however, transmit efficiency in the prostate at 10.5T was down to 62% from approximately 80% at 7T. Decreasing transmit efficiency also resulted in decreased SAR efficiency, which, along with a limited peak B_1^+, made it difficult to obtain some standard contrasts in the hip such as bright fluid signals that are typically provided by dual-echo steady-state type sequences (i.e. DESS) (61). An important point, however, is that clinical imaging of the hip at 3T is usually performed unilaterally, a strategy that would make RF optimization at 10.5T more straightforward.

The limitations of phase shimming were not surprising in larger anatomies such as the liver, heart, and kidney. For these targets, phase-only solutions failed to provide sufficient B_1^+ for the entire ROI. One could in fact observe the limitation from the post-shimming B_1^+ efficiency maps (Figure 1), where phase-only solutions yielded only a narrow band with high efficiency sufficient for the prostate. These limitations can be addressed by using single-spoke or multi-spoke pTx pulses. However, at the present time very few imaging sequences are currently enabled to take advantage of multi-spoke pulses. It is worth noting that the in vivo imaging results were consistent with predictions where the excitation fidelity of a two-spoke pTx pulse greatly improved upon the solution of a single-spoke pulse. These observations suggest that the increased B_1^+ inhomogeneity at 10.5T is predictable and manageable, and that the previously developed methods for imaging at 7T show reasonable translational potential for enabling torso imaging at 10.5T.

With increasing field strength, the compromise between transmit efficiency, SAR efficiency, and transmit homogeneity becomes an increasing limitation for certain acquisitions. These constraints can be tackled through improved transmit chain and RF coil performance and/or through better pTx RF management strategies. For example, the low peak B_1^+ is generally not a major limiting factor for small flip angle imaging. However, it may significantly affect the performance of refocusing and inversion pulses, and, consequently, the image contrast and SNR as observed in the two example TSE imaging series acquired in the prostate (Supporting Information Figure S3). Previous work has shown the feasibility of designing a tailored refocusing or inversion pulse using pTx (64,65) and achieving finer adjustment of B_1^+ inhomogeneity and RF peak and average power in the presence of local or global SAR constraints (66–69). At 10.5T, the use of such tailored pTx pulses is imperative and should be an available alternative to conventional pulses when the latter may not be feasible due to the known limitations of static phase shimming. To design and effectively implement pulses with SAR constraints requires confidence in the simulations used to estimate those values. Typically, virtual observation points (VOPs) are employed to help reduce the computational burden for such calculations (70). Similarly, on the scanner, VOPs and real-time power monitoring hardware can also be implemented to further extend acquisition flexibility.

Developing the confidence in human body models that allows for taking advantage of local SAR control will be critical to fully exploit the pTx system capabilities at UHF and becomes even more imperative at 10.5T.

Besides the static phase shimming and pTx tailored pulses, there are other techniques that may be useful to mitigate B_1^+ inhomogeneity at 10.5T, such as TIAMO (71) and PnP-MR fingerprinting (72). By treating complementary B_1^+ profiles as virtual receive channels, TIAMO uses a GRAPPA reconstruction to yield more homogeneous images at little cost to SNR and SAR (71). The phase configurations used by TIAMO can be predefined empirically. Although less suitable for quantitative imaging, TIAMO may still serve as a calibration-free alternative when static RF shimming is insufficient for imaging large organs such as the liver, and for fast B_1^+ estimation (73). For quantitative imaging, especially T2 mapping at 10.5T, alternative parametric mapping methods such as PnP-MR fingerprinting may be less power demanding as the T2 contrast comes from both the spin echo and stimulated echo pathways and does not require a perfect 180 degree refocusing pulse, although prospective studies are needed to validate quantification accuracy.

While this preliminary study demonstrates the feasibility of obtaining high quality images of the human torso using current RF management methods at 10.5T, quantitative comparisons against 7T are warranted. Such comparisons will require additional attention to the equivalency of the receive chain architecture, including the RF coil. By developing transceiver arrays with higher numbers of transmit channels for 10.5T using dipoles or other relevant resonant structures, increases in peak B_1^+ and SNR are expected (74). For particular torso targets, such coil developments may also be sufficient to minimize the current limitations observed at 10.5T by providing competitive SNR performance compared to RF coils used at 7T. In the case of the prostate, it may be possible to achieve SNRs with the use of a body coil alone at 10.5T that approaches that of 7T studies acquired with an endorectal coil (75–77). Note that high resolution imaging enabled by SNR increases is often accompanied by longer acquisition times and possibly higher power deposition due to the image orientations needed to reduce motion artifacts and the requirement to encode all spins in the slice/volume of excitation. However, the more complex B_1^+ pattern at higher fields improves the spatial encoding capability, which, together with the SNR gain, can improve the parallel imaging performance, leading to a reduction in acquisition time. On the transmit side, the acquisition time may also be reduced by employing reduced field of view excitations, where only spins within regions of interest are excited and spatially encoded by using parallel transmission and multi-dimensional selective pulses (78–80). This may be especially useful for body applications where target anatomies are small compared to the full extent of the body in the plane of the imaging slice.

In the absence of a direct experimental comparison with 7T, the results presented here can be put into context by comparing against previously published work. The manuscript introducing the presently used coil involved simulations with a similar 10 channel dipole array optimized for 7T (43). In that work, phase shimming and spoke pulse designs were used to assess the relative performance between the two field strengths. With respect to the phase only simulations in the prostate, 10.5T simulations predicted slightly higher power efficiency ($\mu T/W^{0.5}$) and SAR efficiency but with higher inhomogeneity with CVs more than

doubled at 10.5T. Experimentally these simulation results are partially corroborated by comparing the current 10.5T with previous results obtained with a 10 channel dipole array at 7T where the CV at 7T was half that of 10.5T in the prostate (i.e. 7% at 7T and 13% at 10.5T) (39). With respect to spoke pulses, simulation showed that for the same anatomical target and number of spokes, peak local SAR increased by 25–35% for prostate, 60–80% for kidneys, and 50–90% for heart with comparable excitation fidelity at 10.5T. However, for the kidneys and heart, designing two-spoke pulses at 10.5T appeared to yield similar performance to single-spoke designs at 7T. For prostate, designing two-spoke pulses at 10.5T started to outperform the single-spoke design at 7T. Verification of these previous simulations and other quantitative field strength comparisons will need to be performed in future target specific studies.

Despite showing the effectiveness of RF management strategies at 10.5T, this study had several limitations. First, to adhere to the time limit allowed by the FDA approved protocol, the actual scanning lasted no more than one hour, restricting the time usable for high-quality acquisitions. Second, due to the limited extent of the RF coil in the foot-head direction and the fact the study protocol did not permit repositioning the coil, targets including the liver and the heart may have been imaged with sub-optimal coil coverage resulting in degraded imaging performance in the superior or inferior aspects of the anatomy. Third, at the time of this study, the pTx functionality required off-line RF shimming and pulse calculations and associated troubleshooting thus lowering the acquisition efficiency during the limited time allotted for imaging. Streamlining pTx functionality in the software system will be critical to promoting pTx in future prospective studies.

CONCLUSION

In this study, we present the first ever in vivo human imaging studies at 10.5T (447MHz). Previously developed RF management strategies for imaging at 7T, including phase-only RF shimming and pTx spoke pulses, have been shown to be effective at tackling the B_1^+ inhomogeneity at 10.5T, allowing high quality images to be acquired in multiple target anatomies throughout the human torso. It is evident, however, that further development and integration of pTx functionality, such as target specific RF pulses, are needed to achieve more uniform transmit B1 fields while optimizing for SAR efficiency since both peak B_1^+ and local SAR were factors limiting the demonstrated applications. When combined with further improvements in the transmit chain efficiency, antenna technology, and local SAR monitoring, proton applications in the human torso at 10.5T are expected to confirm the unique advantages that the increase in field strength can provide.

Supplementary Material

Refer to Web version on PubMed Central for supplementary material.

ACKNOWLEDGEMENTS

The authors would like to acknowledge support from the following funding sources: NIBIB P41 EB015894, NIBIB P41 EB027061 and NIH S10 RR029672.

REFERENCES

1. Vaughan JT, Garwood M, Collins CM, Liu W, DelaBarre L, Adriany G, Andersen P, Merkle H, Goebel R, Smith MB, Ugurbil K. 7T vs. 4T: RF power, homogeneity, and signal-to-noise comparison in head images. Magnetic resonance in medicine : official journal of the Society of Magnetic Resonance in Medicine / Society of Magnetic Resonance in Medicine 2001;46(1):24–30.
2. Vaughan JT, Snyder CJ, DelaBarre LJ, Bolan PJ, Tian J, Bolinger L, Adriany G, Andersen P, Strupp J, Ugurbil K. Whole-body imaging at 7T: preliminary results. Magn Reson Med 2009;61(1):244–248. [PubMed: 19097214]
3. Deelchand DK, Van de Moortele PF, Adriany G, Iltis I, Andersen P, Strupp JP, Vaughan JT, Ugurbil K, Henry PG. In vivo 1H NMR spectroscopy of the human brain at 9.4 T: initial results. J Magn Reson 2010;206(1):74–80. [PubMed: 20598925]
4. Budde J, Shajan G, Hoffmann J, Ugurbil K, Pohmann R. Human imaging at 9.4 T using T(2) *-, phase-, and susceptibility-weighted contrast. Magn Reson Med 2011;65(2):544–550. [PubMed: 20872858]
5. Robitaille PM, Abduljalil AM, Kangarlu A. Ultra high resolution imaging of the human head at 8 tesla: 2K x 2K for Y2K. J Comput Assist Tomogr 2000;24(1):2–8. [PubMed: 10667650]
6. Atkinson IC, Thulborn KR. Feasibility of mapping the tissue mass corrected bioscale of cerebral metabolic rate of oxygen consumption using 17-oxygen and 23-sodium MR imaging in a human brain at 9.4 T. NeuroImage 2010;51(2):723–733. [PubMed: 20188194]
7. Juras V, Mlynarik V, Szomolanyi P, Valkovic L, Trattnig S. Magnetic Resonance Imaging of the Musculoskeletal System at 7T: Morphological Imaging and Beyond. Top Magn Reson Imaging 2019;28(3):125–135. [PubMed: 30951006]
8. Erturk MA, Li X, Van de Moortele PF, Ugurbil K, Metzger GJ. Evolution of UHF Body Imaging in the Human Torso at 7T: Technology, Applications, and Future Directions. Top Magn Reson Imaging 2019;28(3):101–124. [PubMed: 31188271]
9. Guerin B, Villena JF, Polimeridis AG, Adalsteinsson E, Daniel L, White JK, Wald LL. The ultimate signal-to-noise ratio in realistic body models. Magnetic resonance in medicine : official journal of the Society of Magnetic Resonance in Medicine / Society of Magnetic Resonance in Medicine 2017;78(5):1969–1980.
10. Wiesinger F, Van de Moortele PF, Adriany G, De Zanche N, Ugurbil K, Pruessmann KP. Parallel imaging performance as a function of field strength--an experimental investigation using electrodynamic scaling. Magn Reson Med 2004;52(5):953–964. [PubMed: 15508167]
11. Ohliger MA, Grant AK, Sodickson DK. Ultimate intrinsic signal-to-noise ratio for parallel MRI: electromagnetic field considerations. Magnetic resonance in medicine : official journal of the Society of Magnetic Resonance in Medicine / Society of Magnetic Resonance in Medicine 2003;50(5):1018–1030.
12. Tkac I, Andersen P, Adriany G, Merkle H, Ugurbil K, Gruetter R. In vivo (1)H NMR spectroscopy of the human brain at 7 T. Magnetic resonance in medicine : official journal of the Society of Magnetic Resonance in Medicine / Society of Magnetic Resonance in Medicine 2001;46(3):451–456.
13. Tkac I, Oz G, Adriany G, Ugurbil K, Gruetter R. In vivo 1H NMR spectroscopy of the human brain at high magnetic fields: metabolite quantification at 4T vs. 7T. Magn Reson Med 2009;62(4):868–879. [PubMed: 19591201]
14. Koopmans PJ, Manniesing R, Niessen WJ, Viergever MA, Barth M. MR venography of the human brain using susceptibility weighted imaging at very high field strength. MAGMA 2008;21(1–2):149–158. [PubMed: 18188626]
15. Abosch A, Yacoub E, Ugurbil K, Harel N. An assessment of current brain targets for deep brain stimulation surgery with susceptibility-weighted imaging at 7 tesla. Neurosurgery 2010;67(6):1745–1756; discussion 1756. [PubMed: 21107206]
16. Bian W, Hess CP, Chang SM, Nelson SJ, Lupo JM. Susceptibility-weighted MR imaging of radiation therapy-induced cerebral microbleeds in patients with glioma: a comparison between 3T and 7T. Neuroradiology 2014;56(2):91–96. [PubMed: 24281386]

17. Ugurbil K Imaging at ultrahigh magnetic fields: History, challenges, and solutions. Neuroimage 2018;168:7–32. [PubMed: 28698108]

18. Adriany G, Van de Moortele PF, Wiesinger F, Moeller S, Strupp JP, Andersen P, Snyder C, Zhang X, Chen W, Pruessmann KP, Boesiger P, Vaughan T, Ugurbil K. Transmit and receive transmission line arrays for 7 Tesla parallel imaging. Magn Reson Med 2005;53(2):434–445. [PubMed: 15678527]

19. Van de Moortele PF, Akgun C, Adriany G, Moeller S, Ritter J, Collins CM, Smith MB, Vaughan JT, Ugurbil K. B(1) destructive interferences and spatial phase patterns at 7 T with a head transceiver array coil. Magn Reson Med 2005;54(6):1503–1518. [PubMed: 16270333]

20. Ugurbil K Magnetic resonance imaging at ultrahigh fields. IEEE transactions on biomedical engineering 2014;61(5):1364–1379. [PubMed: 24686229]

21. Vaughan TJ, Ugurbil K, Adriany G; Reagents of the University of Minnesota, assignee. Radiofrequency, Gradient, shim, and Parallel Imaging Coil. United States patent Number 7,598,739. 2003.

22. Snyder CJ, DelaBarre L, Metzger GJ, van de Moortele PF, Akgun C, Ugurbil K, Vaughan JT. Initial results of cardiac imaging at 7 Tesla. Magn Reson Med 2009;61(3):517–524. [PubMed: 19097233]

23. Suttie JJ, Delabarre L, Pitcher A, van de Moortele PF, Dass S, Snyder CJ, Francis JM, Metzger GJ, Weale P, Ugurbil K, Neubauer S, Robson M, Vaughan T. 7 Tesla (T) human cardiovascular magnetic resonance imaging using FLASH and SSFP to assess cardiac function: validation against 1.5 T and 3 T. NMR in biomedicine 2012;25(1):27–34. [PubMed: 21774009]

24. Schmitter S, Delabarre L, Wu X, Greiser A, Wang D, Auerbach EJ, Vaughan JT, Ugurbil K, Van de Moortele PF. Cardiac imaging at 7 tesla: Single- and two-spoke radiofrequency pulse design with 16-channel parallel excitation. Magn Reson Med 2013;70(5):1210–1219. [PubMed: 24038314]

25. Zhang Z, Yip CY, Grissom W, Noll DC, Boada FE, Stenger VA. Reduction of transmitter B1 inhomogeneity with transmit SENSE slice-select pulses. Magn Reson Med 2007;57(5):842–847. [PubMed: 17457863]

26. Katscher U, Bornert P, Leussler C, van den Brink JS. Transmit SENSE. Magn Reson Med 2003;49(1):144–150. [PubMed: 12509830]

27. Katscher U, Bornert P, van den Brink JS. Theoretical and numerical aspects of transmit SENSE. IEEE Trans Med Imaging 2004;23(4):520–525. [PubMed: 15084077]

28. Grissom W, Yip CY, Zhang Z, Stenger VA, Fessler JA, Noll DC. Spatial domain method for the design of RF pulses in multicoil parallel excitation. Magn Reson Med 2006;56(3):620–629. [PubMed: 16894579]

29. Jankiewicz M, Zeng H, Moore JE, Anderson AW, Avison MJ, Welch EB, Gore JC. Practical considerations for the design of sparse-spokes pulses. J Magn Reson 2010;203(2):294–304. [PubMed: 20172754]

30. Cloos MA, Luong M, Ferrand G, Amadon A, Le Bihan D, Boulant N. Local SAR reduction in parallel excitation based on channel-dependent Tikhonov parameters. J Magn Reson Imaging 2010;32(5):1209–1216. [PubMed: 21031527]

31. Setsompop K, Alagappan V, Gagoski BA, Potthast A, Hebrank F, Fontius U, Schmitt F, Wald LL, Adalsteinsson E. Broadband slab selection with B1+ mitigation at 7T via parallel spectral-spatial excitation. Magnetic resonance in medicine : official journal of the Society of Magnetic Resonance in Medicine / Society of Magnetic Resonance in Medicine 2009;61(2):493–500.

32. Zelinski AC, Wald LL, Setsompop K, Alagappan V, Gagoski BA, Goyal VK, Adalsteinsson E. Fast slice-selective radio-frequency excitation pulses for mitigating B+1 inhomogeneity in the human brain at 7 Tesla. Magnetic resonance in medicine : official journal of the Society of Magnetic Resonance in Medicine / Society of Magnetic Resonance in Medicine 2008;59(6):1355–1364.

33. Cloos MA, Boulant N, Luong M, Ferrand G, Giacomini E, Le Bihan D, Amadon A. kT -points: short three-dimensional tailored RF pulses for flip-angle homogenization over an extended volume. Magn Reson Med 2012;67(1):72–80. [PubMed: 21590724]

34. Hoffmann J, Henning A, Giapitzakis IA, Scheffler K, Shajan G, Pohmann R, Avdievich NI. Safety testing and operational procedures for self-developed radiofrequency coils. NMR in biomedicine 2016;29(9):1131–1144. [PubMed: 25851551]

35. Snyder CJ, DelaBarre L, Tian J, Metzger GJ, Ugurbil K, Vaughan JT. 28-Channel Receive-Only Array For Body Imaging at 7T. Proceedings of the 23rd Annual Meeting of ISMRM, Stockholm, Sweden 2010;18:3829.

36. Rietsch SHG, Orzada S, Maderwald S, Brunheim S, Philips BWJ, Scheenen TWJ, Ladd ME, Quick HH. 7T ultra-high field body MR imaging with an 8-channel transmit/32-channel receive radiofrequency coil array. Med Phys 2018;45(7):2978–2990. [PubMed: 29679498]

37. Steensma BR, Voogt IJ, Leiner T, Luijten PR, Habets J, Klomp DWJ, van den Berg CAT, Raaijmakers AJE. An 8-channel Tx/Rx dipole array combined with 16 Rx loops for high-resolution functional cardiac imaging at 7 T. MAGMA 2018;31(1):7–18. [PubMed: 29177772]

38. Voogt IJ, Klomp DW, Hoogduin JM, Luttje MP, Luijten PR, Van den Berg CA, Raaijmakers AJ. Combined 8-channel transceiver fractionated dipole antenna array with a 16-channel loop coil receive array for body imaging at 7 Tesla. Proc Intl Soc Mag Reson Med. Volume 23 Toronto, Ontario, Canada2015. p 631.

39. Erturk MA, Raaijmakers AJ, Adriany G, Ugurbil K, Metzger GJ. A 16-channel combined loop-dipole transceiver array for 7 Tesla body MRI. Magn Reson Med 2017;77(2):884–894. [PubMed: 26887533]

40. Oezerdem C, Winter L, Graessl A, Paul K, Els A, Weinberger O, Rieger J, Kuehne A, Dieringer M, Hezel F, Voit D, Frahm J, Niendorf T. 16-channel bow tie antenna transceiver array for cardiac MR at 7.0 tesla. Magn Reson Med 2016;75(6):2553–2565. [PubMed: 26183320]

41. Graessl A, Renz W, Hezel F, Dieringer MA, Winter L, Oezerdem C, Rieger J, Kellman P, Santoro D, Lindel TD, Frauenrath T, Pfeiffer H, Niendorf T. Modular 32-channel transceiver coil array for cardiac MRI at 7.0T. Magn Reson Med 2014;72(1):276–290. [PubMed: 23904404]

42. Raaijmakers AJ, Italiaander M, Voogt IJ, Luijten PR, Hoogduin JM, Klomp DW, van den Berg CA. The fractionated dipole antenna: A new antenna for body imaging at 7 Tesla. Magn Reson Med 2016;75(3):1366–1374. [PubMed: 25939890]

43. Erturk MA, Wu XP, Eryaman Y, Van de Moortele PF, Auerbach EJ, Lagore RL, DelaBarre L, Vaughan JT, Ugurbil K, Adriany G, Metzger GJ. Toward imaging the body at 10.5 tesla. Magnet Reson Med 2017;77(1):434–443.

44. Heilmaier C, Theysohn JM, Maderwald S, Kraff O, Ladd ME, Ladd SC. A large-scale study on subjective perception of discomfort during 7 and 1.5 T MRI examinations. Bioelectromagnetics 2011;32(8):610–619. [PubMed: 21598286]

45. Roberts DC, Marcelli V, Gillen JS, Carey JP, Della Santina CC, Zee DS. MRI magnetic field stimulates rotational sensors of the brain. Curr Biol 2011;21(19):1635–1640. [PubMed: 21945276]

46. Theysohn JM, Kraff O, Eilers K, Andrade D, Gerwig M, Timmann D, Schmitt F, Ladd ME, Ladd SC, Bitz AK. Vestibular effects of a 7 Tesla MRI examination compared to 1.5 T and 0 T in healthy volunteers. PLoS One 2014;9(3):e92104. [PubMed: 24658179]

47. Ward BK, Roberts DC, Della Santina CC, Carey JP, Zee DS. Vestibular stimulation by magnetic fields. Ann N Y Acad Sci 2015;1343:69–79. [PubMed: 25735662]

48. Van de Moortele PF, Snyder C, DelaBarre L, Akgun C, Wu X, Vaughan JT, Ugurbil K. Fast Mapping of Relative B1+ Phase in the Human Head at 9.4 Tesla with a 14 Channel Transceive Coil Array. International Symposium on Biomedical Magnetic Resonance Imaging and Spectroscopy at Very High Fields, Wruzburg, Germany 2006.

49. Van de Moortele PF, Snyder C, DelaBarre L, Adriany G, Vaughan JT, Ugurbil K. Calibration Tools for RF Shim at Very High Field with Multiple Element RF Coils: from Ultra Fast Local Relative Phase to Absolute Magnitude B1+ Mapping. Proc Intl Soc Mag Reson Med. Volume 15 Berlin, Germany 2007 p 1676.

50. Van de Moortele P, Ugurbil K. Very Fast Multi Channel B1 Calibration at High Field in the Small Flip Angle Regime. Proc Intl Soc Mag Reson Med. Volume 17 Honolulu, Hawaii, USA 2009 p 367.

51. Metzger GJ, Auerbach EJ, Akgun C, Simonson J, Bi X, Ugurbil K, van de Moortele PF. Dynamically applied B1+ shimming solutions for non-contrast enhanced renal angiography at 7.0 Tesla. Magn Reson Med 2013;69(1):114–126. [PubMed: 22442056]

52. Setsompop K, Alagappan V, Gagoski B, Witzel T, Polimeni J, Potthast A, Hebrank F, Fontius U, Schmitt F, Wald LL, Adalsteinsson E. Slice-selective RF pulses for in vivo B1+ inhomogeneity

mitigation at 7 tesla using parallel RF excitation with a 16-element coil. Magn Reson Med 2008;60(6):1422–1432. [PubMed: 19025908]

53. Hansen PC. Regularization tools version 4.0 for matlab 7.3. Numer Algorithms 2007;46(2):189–194.
54. Wu X, Schmitter S, Auerbach EJ, Ugurbil K, Van de Moortele PF. Mitigating transmit B 1 inhomogeneity in the liver at 7T using multi-spoke parallel transmit RF pulse design. Quant Imaging Med Surg 2014;4(1):4–10. [PubMed: 24649429]
55. Yarnykh VL. Actual flip-angle imaging in the pulsed steady state: a method for rapid three-dimensional mapping of the transmitted radiofrequency field. Magn Reson Med 2007;57(1):192–200. [PubMed: 17191242]
56. International Electrotechnical Commission (IEC). Particular requirements for the safety of magnetic resonance equipment for medical diagnosis. International Standard IEC 60601–2–33 2010.
57. Alon L, Deniz CM, Carluccio G, Brown R, Sodickson DK, Collins CM. Effects of Anatomical Differences on Electromagnetic Fields, SAR, and Temperature Change. Concepts Magn Reson Part B Magn Reson Eng 2016;46(1):8–18. [PubMed: 27134586]
58. van den Bergen B, van den Berg CA, Klomp DW, Lagendijk JJ. SAR and power implications of different RF shimming strategies in the pelvis for 7T MRI. Journal of magnetic resonance imaging : JMRI 2009;30(1):194–202. [PubMed: 19557737]
59. Schmid MR, Pfirrmann CW, Koch P, Zanetti M, Kuehn B, Hodler J. Imaging of patellar cartilage with a 2D multiple-echo data image combination sequence. AJR Am J Roentgenol 2005;184(6):1744–1748. [PubMed: 15908524]
60. Frauenrath T, Hezel F, Renz W, d'Orth Tde G, Dieringer M, von Knobelsdorff-Brenkenhoff F, Prothmann M, Schulz Menger J, Niendorf T. Acoustic cardiac triggering: a practical solution for synchronization and gating of cardiovascular magnetic resonance at 7 Tesla. Journal of cardiovascular magnetic resonance : official journal of the Society for Cardiovascular Magnetic Resonance 2010;12:67. [PubMed: 21080933]
61. Ellermann J, Goerke U, Morgan P, Ugurbil K, Tian J, Schmitter S, Vaughan T, Van De Moortele PF. Simultaneous bilateral hip joint imaging at 7 Tesla using fast transmit B(1) shimming methods and multichannel transmission - a feasibility study. NMR Biomed 2012;25(10):1202–1208. [PubMed: 22311346]
62. Maas MC, Vos EK, Lagemaat MW, Bitz AK, Orzada S, Kobus T, Kraff O, Maderwald S, Ladd ME, Scheenen TW. Feasibility of T2 -weighted turbo spin echo imaging of the human prostate at 7 tesla. Magn Reson Med 2014;71(5):1711–1719. [PubMed: 23798333]
63. Metzger GJ, Kalavagunta C, Spilseth B, Bolan PJ, Li X, Hutter D, Nam JW, Johnson AD, Henriksen JC, Moench L, Konety B, Warlick CA, Schmechel SC, Koopmeiners JS. Detection of Prostate Cancer: Quantitative Multiparametric MR Imaging Models Developed Using Registered Correlative Histopathology. Radiology 2016;279(3):805–816. [PubMed: 26761720]
64. Massire A, Cloos MA, Vignaud A, Le Bihan D, Amadon A, Boulant N. Design of non-selective refocusing pulses with phase-free rotation axis by gradient ascent pulse engineering algorithm in parallel transmission at 7T. J Magn Reson 2013;230:76–83. [PubMed: 23454576]
65. Xu D, King KF, Zhu Y, McKinnon GC, Liang ZP. Designing multichannel, multidimensional, arbitrary flip angle RF pulses using an optimal control approach. Magn Reson Med 2008;59(3):547–560. [PubMed: 18306407]
66. Zhu Y Parallel excitation with an array of transmit coils. Magn Reson Med 2004;51(4):775–784. [PubMed: 15065251]
67. Guerin B, Gebhardt M, Cauley S, Adalsteinsson E, Wald LL. Local specific absorption rate (SAR), global SAR, transmitter power, and excitation accuracy trade-offs in low flip-angle parallel transmit pulse design. Magn Reson Med 2014;71(4):1446–1457. [PubMed: 23776100]
68. Guerin B, Setsompop K, Ye H, Poser BA, Stenger AV, Wald LL. Design of parallel transmission pulses for simultaneous multislice with explicit control for peak power and local specific absorption rate. Magn Reson Med 2015;73(5):1946–1953. [PubMed: 24938991]
69. Lee J, Gebhardt M, Wald LL, Adalsteinsson E. Local SAR in parallel transmission pulse design. Magn Reson Med 2012;67(6):1566–1578. [PubMed: 22083594]

70. Eichfelder G, Gebhardt M. Local specific absorption rate control for parallel transmission by virtual observation points. Magn Reson Med 2011;66(5):1468–1476. [PubMed: 21604294]
71. Orzada S, Maderwald S, Poser BA, Bitz AK, Quick HH, Ladd ME. RF excitation using time interleaved acquisition of modes (TIAMO) to address B1 inhomogeneity in high-field MRI. Magn Reson Med 2010;64(2):327–333. [PubMed: 20574991]
72. Cloos MA, Knoll F, Zhao T, Block KT, Bruno M, Wiggins GC, Sodickson DK. Multiparametric imaging with heterogeneous radiofrequency fields. Nat Commun 2016;7:12445. [PubMed: 27526996]
73. Brunheim S, Gratz M, Johst S, Bitz AK, Fiedler TM, Ladd ME, Quick HH, Orzada S. Fast and accurate multi-channel B1+ mapping based on the TIAMO technique for 7T UHF body MRI. Magn Reson Med 2018;79(5):2652–2664. [PubMed: 28994132]
74. Snyder CJ, Delabarre L, Moeller S, Tian J, Akgun C, Van de Moortele PF, Bolan PJ, Ugurbil K, Vaughan JT, Metzger GJ. Comparison between eight- and sixteen-channel TEM transceive arrays for body imaging at 7 T. Magnetic resonance in medicine 2012;67(4):954–964. [PubMed: 22102483]
75. Erturk MA, Tian J, Van de Moortele PF, Adriany G, Metzger GJ. Development and evaluation of a multichannel endorectal RF coil for prostate MRI at 7T in combination with an external surface array. J Magn Reson Imaging 2016;43(6):1279–1287. [PubMed: 26584144]
76. Metzger GJ, van de Moortele PF, Akgun C, Snyder CJ, Moeller S, Strupp J, Andersen P, Shrivastava D, Vaughan T, Ugurbil K, Adriany G. Performance of external and internal coil configurations for prostate investigations at 7 T. Magn Reson Med 2010;64(6):1625–1639. [PubMed: 20740657]
77. Arteaga de Castro CS, van den Bergen B, Luijten PR, van der Heide UA, van Vulpen M, Klomp DW. Improving SNR and B1 transmit field for an endorectal coil in 7 T MRI and MRS of prostate cancer. Magnetic resonance in medicine 2012;68(1):311–318. [PubMed: 22127763]
78. Jang A, Wu X, Auerbach EJ, Garwood M. Designing 3D selective adiabatic radiofrequency pulses with single and parallel transmission. Magnetic resonance in medicine : official journal of the Society of Magnetic Resonance in Medicine / Society of Magnetic Resonance in Medicine 2018;79(2):701–710. [PubMed: 28497465]
79. Schulte RF, Wiesinger F. Direct design of 2D RF pulses using matrix inversion. J Magn Reson 2013;235:115–120. [PubMed: 24013595]
80. Jang A, Kobayashi N, Moeller S, Vaughan JT, Zhang J, Garwood M. 2D Pulses using spatially dependent frequency sweeping. Magn Reson Med 2016;76(5):1364–1374. [PubMed: 26614693]

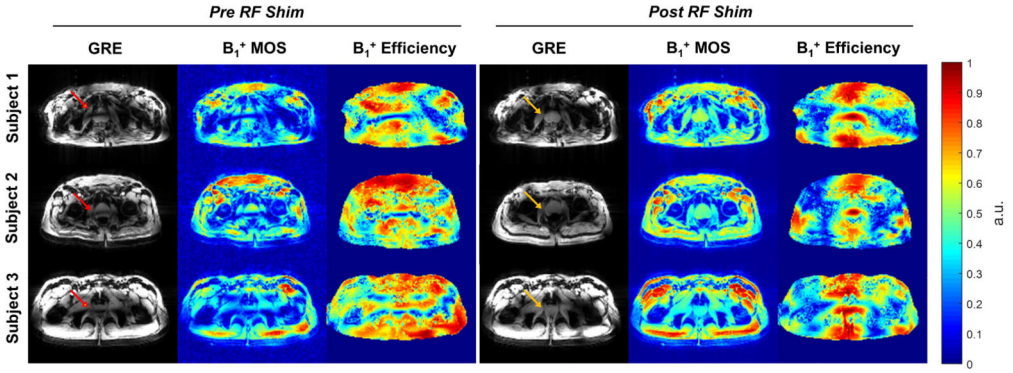

Figure 1.

The acquired low-flip angle GRE images and the simulated B_1^+ spatial profiles and efficiency maps in the prostates of three subjects before and after phase-only RF shimming. The simulated B_1^+ MOS images matched closely with acquired images in terms of the spatially varying B_1^+ (note that the acquired images include receive profile information). The B_1^+ efficiency and homogeneity were improved in the prostate after RF shimming (yellow arrows) compared to the pre-shimming results (red arrows). Note that the simulated B_1^+ MOS image is proton density weighted and that the B_1^+ efficiency maps are masked to exclude the background noise.

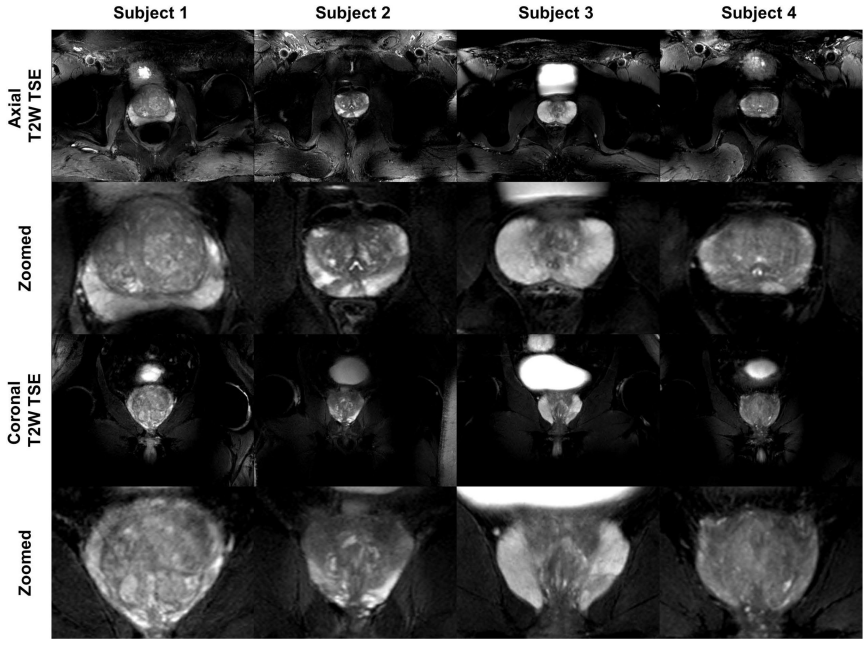

Figure 2.

Full field of view and zoomed in versions of axial and coronal T_2W TSE images of prostates from four subjects. The images demonstrate excellent contrast and SNR achieved by phase-only RF shimming. While providing high peak B_1^+ and reasonable homogeneity over the prostate, the local RF shim resulted in unmanaged RF fields outside the immediate region of the targeted anatomy that caused spatially varying destructive interference patterns as observed in the un-zoomed images.

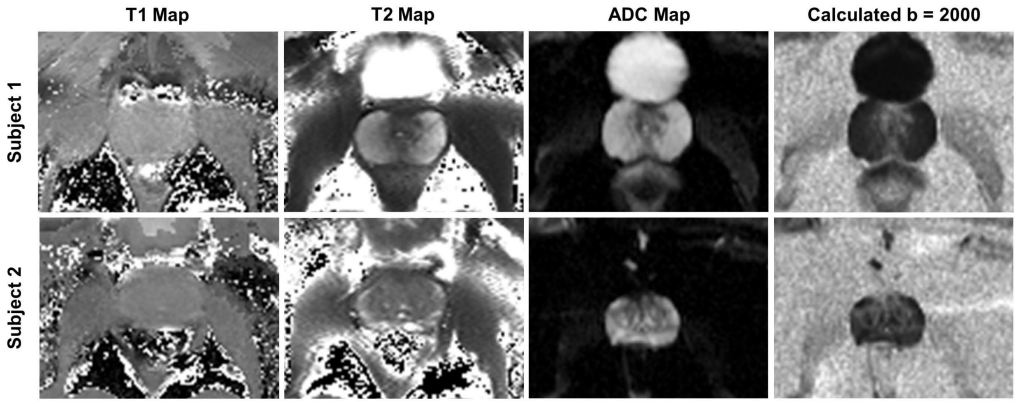

Figure 3.

Zoomed-in parametric maps of the prostate including T_1, T_2, ADC, and calculated high b-value DWI (b = 2000) generated from IR-FLASH, multi-echo spin echo (SEMC) and SE-EPI DWI acquisitions. This study demonstrates the feasibility of performing quantitative imaging at 10.5T and imaging with diagnostically relevant sequences for this anatomy.

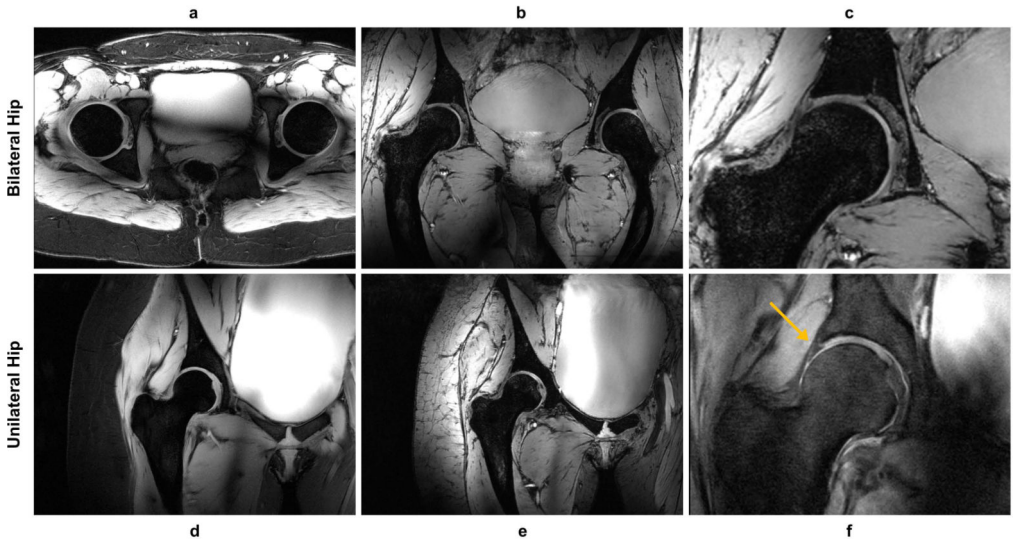

Figure 4.

Examples of hip images acquired with different contrasts. For the bilateral hip, 2D axial GRE (a), 3D coronal MEDIC (b), and a zoomed version of the MEDIC acquisition (c) are shown. For the unilateral hip, 2D coronal GRE (d), 3D coronal MEDIC (e), and PD weighted TSE (f) images are shown with the latter showing the expected contrast between the labrum and cartilage (yellow arrow). (a), (d), (f) were acquired with lipid suppression and demonstrated excellent performance and contrast.

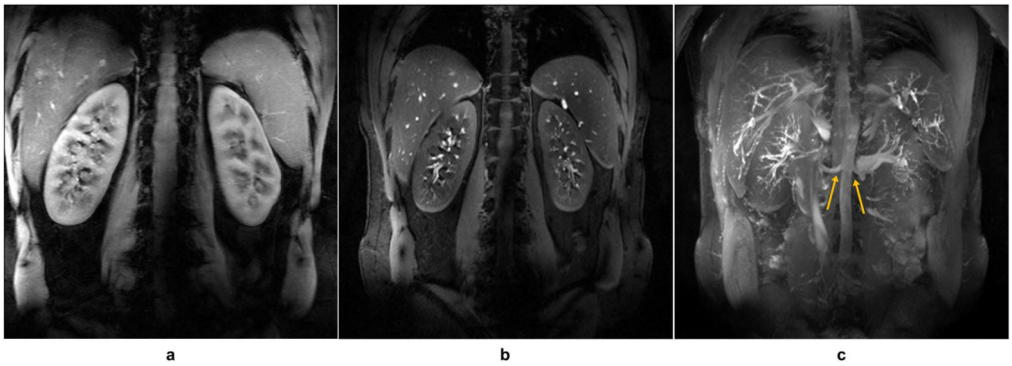

Figure 5.

Example of breath-hold renal images acquired with lipid suppression including a 2D coronal anatomic GRE (a) and an inflow-enhanced acquisition (b). (c) Maximum intensity projection (MIP) across the stack of images represented in (b) demonstrates the high inflow-enhancement and background suppression afforded by the increased T1 of tissues and blood at 10.5T. After phase-only shimming, a relatively uniform signal intensity was achieved in the oblique coronal plane over which these images were acquired. The origins of renal arteries are well visualized on the MIP image (yellow arrows), while distal arterial branches can also be appreciated.

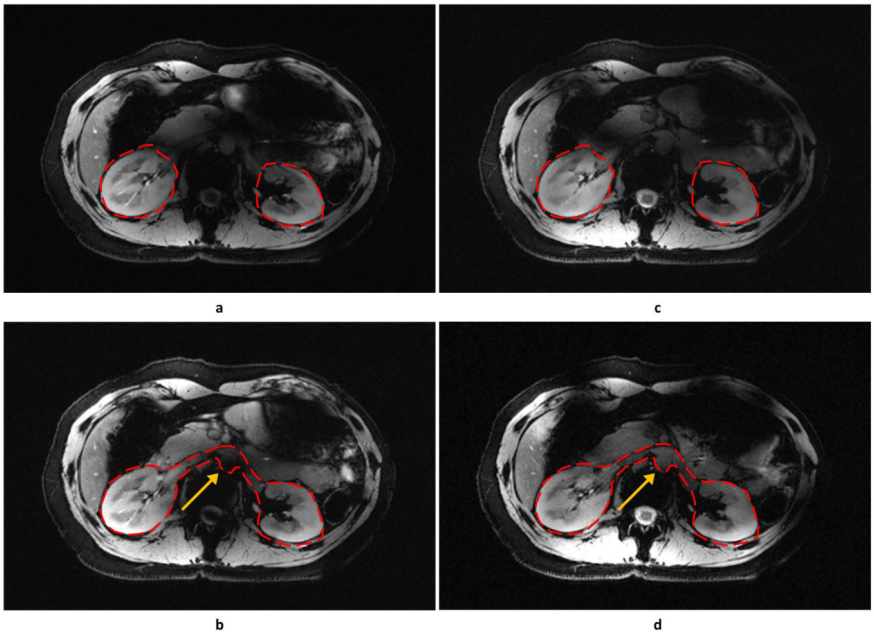

Figure 6.

Example of fat-saturated, breath-hold 2D axial GRE images of the kidney using different RF management strategies. Shimming ROIs are illustrated by red dashed lines. Static phase-only RF shimming was used in (a) and (b) while single-spoke pTx pulses were used in (c) and (d). Compared with phase-only shimming in the smaller ROI (a), the single-spoke pTx pulse (c) showed similar performance in mitigating B_1^+ inhomogeneity. For the larger ROI, the single-spoke pTx pulse (d) was more effective than the phase-only solution (b) against B_1^+ inhomogeneity as indicated by the yellow arrows.

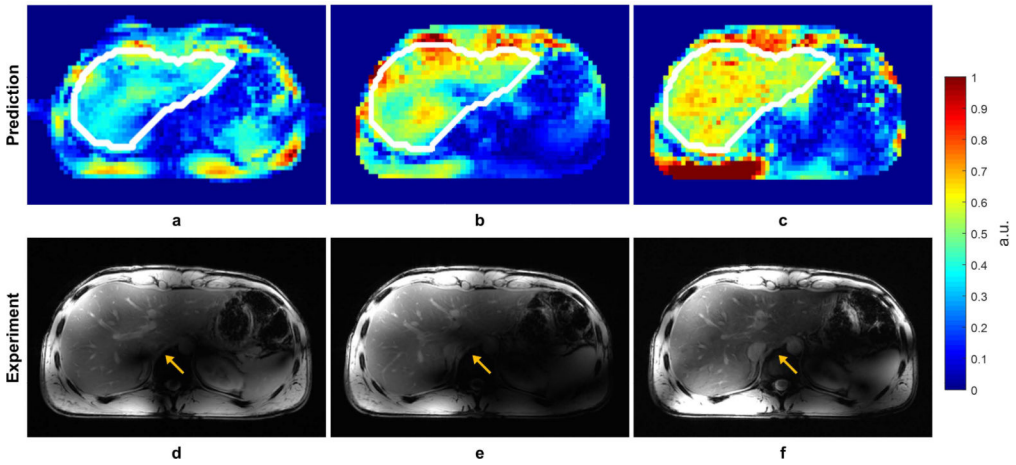

Figure 7.

Predicted B_1^+ profiles (a, b, c) and acquired low-flip angle GRE images (d, e, f) in the liver with different RF management strategies: static phase-only RF shimming with a homogeneity cost function (a, d); single-spoke pTx pulse (b, e); two-spoke pTx pulse (e, f). The acquired images matched well with prediction in terms of predicted B_1^+ profiles. The two-spoke pTx pulse effectively mitigated the B_1^+ inhomogeneity in the liver as demonstrated by improved consistency in contrast throughout the organ (yellow arrows). Note: the experimental data is weighted by the receive profile of the 10-channel dipole array.

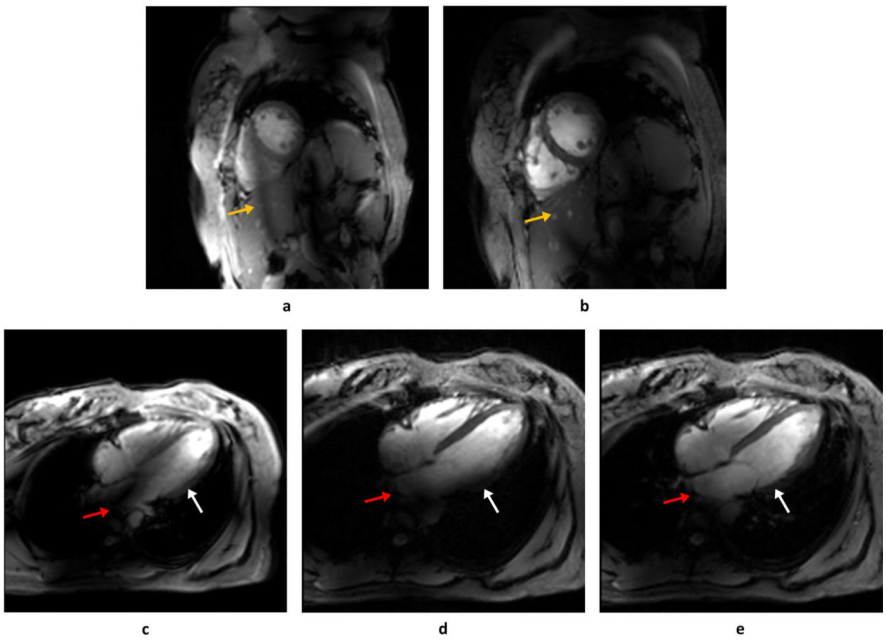

Figure 8.

A single frame during diastole of the cardiac CINE acquisitions in the short-axis (a, b) and four-chamber (c, d, e) views. Images acquired before phase-only RF shimming (a, c) are contrasted with those with phase-only static RF shims (b, d). In the 4-chamber view a single-spoke pTx pulse was also implemented (e). In the short-axis view, phase-only shimming improved the myocardium-blood pool contrast and shifted a band of low B_1^+ outside of the heart (yellow arrows in a, b). However, in the four-chamber view, the phase-only shimming yielded persistent B_1^+ inhomogeneities in the base of the left ventricle (white arrow) and atrium (red arrow) which were addressed with a single-spoke pTx pulse (e).